Quantifying Large Lattice Relaxations in Photovoltaic Devices

Marco Nardone,[1,*] Yasas Patikirige,[1] Kyoung E. Kweon,[2] Curtis Walkons,[3]
Theresa Magorian Friedlmeier,[4] Joel B. Varley,[2] Vincenzo Lordi,[2] and Shubhra Bansal[3]

[1] *Department of Physics and Astronomy, Bowling Green State University, Bowling Green, Ohio 43403, USA*
[2] *Lawrence Livermore National Laboratory, Materials Science Division, Livermore, California 94550, USA*
[3] *Department of Mechanical Engineering, University of Nevada Las Vegas, Las Vegas, Nevada 89154, USA*
[4] *Zentrum für Sonnenenergie- und Wasserstoff-Forschung Baden-Württemberg, Stuttgart, Germany*

(Received 27 October 2019; accepted 17 January 2020; published 11 February 2020)

Temporal variations of Cu(In, Ga)Se_2 photovoltaic device properties during light exposure at various temperatures and voltage biases for times up to 100 h are analyzed using the kinetic theory of large lattice relaxations. Open-circuit voltage and p-type doping increased with charge injection and decreased with temperature at low injection conditions. Lattice relaxation can account for both trends and activation energies extracted from the data are approximately 0.9 and 1.2 eV for devices with lower and higher sodium content, respectively. In these devices, increased sodium content resulted in higher initial p-type doping with greater stability. First-principles calculations providing revised activation energies for the $(V_{\mathrm{Se}} - V_{\mathrm{Cu}})$ complex suggest that this defect does not account for the metastability observed here.

DOI: 10.1103/PhysRevApplied.13.024025

I. INTRODUCTION

Large lattice relaxations (LLR) are changes in local lattice configurations around defects due to coupling between the electronic and atomic systems. These defects are often metastable in that they can undergo thermally activated transitions driven by charge injection, photoexcitation and/or thermal energy and they can return to ground by thermal annealing [1]. Hence, the single defect level picture is insufficient and defect transformations can result in unique, time-dependent electronic properties. Some examples include persistent photoconductivity (PPC) in III-V materials (such as (Al, Ga)As caused by DX and EL2 center defects [2,3]), PPC in II-VI materials (such as CdS [4,5] and CdTe [6]), photodegradation of hydrogenated amorphous silicon (a-Si:H) caused by dangling bond defects [7], charge-induced free carrier lifetime decay in crystalline silicon due to metastable boron-oxygen complexes [8], and impediments to doping of CdTe due to self-compensation by AX centers [9,10]. Fundamental understanding of materials with LLR defects can improve the performance and reliability of semiconductor devices. In this work we present a general approach for quantifying activation energies associated with LLR using *in situ* stress experiments, reaction kinetics analysis, and first-principles calculations. Copper indium gallium diselenide (CIGS) photovoltaic (PV) devices are considered as a specific application.

CIGS solar cells are commercially important with lab-scale power conversion efficiency surpassing 22% [11]. PPC has been observed in polycrystalline CIGS films and attributed to LLR [12]. A related and common observation is the metastable drift of electronic properties over time when exposed to heat, light, and/or voltage bias [13–17]. Typically, the net acceptor (hole) concentration, N, and open-circuit voltage, V_{oc}, increase with temperature under charge injection conditions, whereas dark annealing (without charge injection) tends to reduce N and V_{oc}. Similar effects have been observed in single crystal CIGS PV devices [18].

The microscopic nature of the metastable defect was originally thought to be a negative-U center because it was found by deep-level transient spectroscopy that two electrons are consumed (or holes formed) for every defect created [14]. Later, *ab initio* calculations showed that the $(V_{\mathrm{Se}} - V_{\mathrm{Cu}})$ divacancy complex (with negative-U properties) could exhibit LLR transitions between donor and acceptor configurations [19]; support for this model has been widely cited [20–24]. Experimental support [25,26] for the calculated activation energies from Ref. [19] has been reported for time scales <1000 s. Our results over longer time scales of up to 100 h indicate that a different defect species may be involved. As a first step, we provide revised first-principles energy calculations for the $(V_{\mathrm{Se}} - V_{\mathrm{Cu}})$ complex. Although the revised activation energies are mostly higher than the original ones, they are still rather low compared to those extracted from the data. Alternative defect species must be considered.

*marcon@bgsu.edu

 © 2020 American Physical Society

An important property of high-efficiency CIGS devices is alkali content, which is introduced either by sodium diffusion from the glass substrate or postdeposition treatment with NaF, KF, RbF, and/or CsF. Recently, it was shown that heat and light exposure causes greater acceptor formation in cells with KF [17,27] and RbF [28] than without alkali treatment. It appears that alkali impurities have an effect on LLR transition rates but further study is required. Herein we study CIGS cells with typical sodium content due to diffusion from the soda-lime glass substrate (type 1) and reduced sodium due to a diffusion barrier (type 2).

Our results for V_{oc} as a function of time under light, voltage, and temperature stress are shown in Fig. 1. A unique feature of this data is that performance metrics are measured *in situ* during stress at various temperatures and voltages, enabling a close examination of the time dependence. Most stress tests require intermittent removal of the device under study for measurements. Metastability is evident in Fig. 1 with increasing V_{oc} during high charge injection ($V = V_{oc}$ bias) and decreasing during low charge injection ($V = 0$ bias); the rates of both processes increase with temperature. The solid lines are the LLR model fits, as described below.

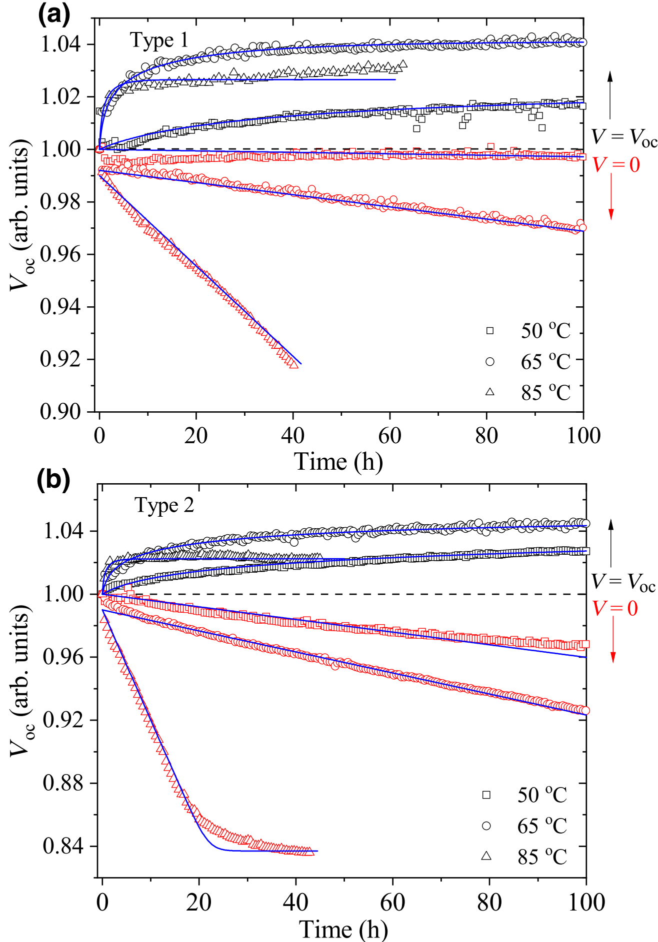

FIG. 1. Open-circuit voltage (V_{oc}) normalized to the initial value as a function of time during stress at 0.1 W/cm^2 light intensity and the indicated voltage biases (0 or V_{oc}) and temperatures for (a) type 1 and (b) type 2 devices. Points are data and lines are model fits from Eq. (9).

II. REACTION KINETICS

Variations in the quasi-Fermi levels (i.e., free carrier concentrations) due to external perturbations lead to changes in the occupancy (charge states) of defects. Certain defects respond by a reorientation of the local the crystal lattice to lower the system energy. These structural relaxations are often thermally activated and can be described using the formalism of chemical reaction kinetics [1]. Defect reactions typically involve capture and/or emission of charge carriers; a single carrier process is a first-order reaction, simultaneous capture of two carriers is second order, and so on. The following subsections describe general first- and second-order reaction kinetics. In Sec. IV, this approach is used to extract activation energies from the data.

A. First-order kinetics

If the LLR process is driven by electron capture and a first-order reaction is assumed, then the kinetics can be described by Ref. [29],

$$\frac{dN}{dt} = \alpha n - \beta N, \tag{1}$$

where N is the defect concentration (reaction product) and n is the *excess* electron concentration. The forward and backward reaction rates are $\alpha = \alpha_0 \exp(-E_\alpha/kT)$ and $\beta = \beta_0 \exp(-E_\beta/kT)$ with activation energies E_α and E_β, Boltzmann constant k, and temperature T. Pre-exponentials α_0 and β_0 are proportional to the characteristics phonon frequency, carrier thermal velocity, capture cross sections, and density of the defects, the details of which are beyond the present scope. α and β are material properties that can also depend on local impurities. Note that electron capture can be interchanged with holes.

The excess electron concentration, n, depends on the defect density, N. If the defects are recombination centers, then the quasistationary approximation, $dn/dt = G - CNn \approx 0$ requires that $n = G/CN$, where G is the generation rate and C is the recombination coefficient. In the case of shallow acceptor defect formation, the mass action law requires that $n = n_i^2\gamma/N$, where n_i is the intrinsic concentration and

$$\gamma = \exp(eU/kT) - 1 \tag{2}$$

defines electron injection through the quasi-Fermi level splitting eU. In both cases, nonequilibrium charge injection invokes an effect to decrease the charge concentration toward equilibrium values, in accordance with Le Chatelier's principle.

Given an initial defect density of N_0 and the above expressions for $n(N)$, Eq. (1) yields,

$$N = N_\infty \sqrt{1 - \left[1 - \left(\frac{N_0}{N_\infty}\right)^2\right] \exp(-2\beta t)}, \quad (3)$$

with a saturation value of,

$$N_\infty = \sqrt{\alpha G / C\beta}, \quad (4)$$

for the case of recombination type defects, and

$$N_\infty = n_i \sqrt{\alpha\gamma/\beta}, \quad (5)$$

for shallow acceptor defects. The saturation level can be higher or lower than the initial concentration. Under low injection conditions, $N_\infty \ll N_0$, and Eq. (3) reduces to

$$N = N_0 \exp(-t/\tau_a) \quad \text{with } \tau_a = 1/\beta. \quad (6)$$

Low injection can also be considered annealing conditions at elevated temperatures in the dark; hence the characteristic annealing time, τ_a. For charge injection conditions but at relatively short times ($t \ll \tau_a$), before the onset of saturation, Eq. (3) can be expressed as

$$N = N_0 \sqrt{1 + t/\tau} \quad \text{with } \tau = \frac{1}{2\beta}\left(\frac{N_0^2}{N_\infty^2 - N_0^2}\right). \quad (7)$$

B. Second-order kinetics

Reaction kinetics for the capture of two electrons can be described by

$$\frac{dN}{dt} = \alpha n^2 - \beta N, \quad (8)$$

with α having units of $cm^{-3}\ s^{-1}$ in this case. Examples of double carrier processes include negative-U, DX, and AX centers, which have been studied in several materials [2,5,30–32]. From Eq. (8) and with the same $n(N)$ dependence described in Sec. II A, defect evolution takes the form,

$$N = N_\infty \left\{1 - \left[1 - \left(\frac{N_0}{N_\infty}\right)^3\right] \exp(-3\beta t)\right\}^{1/3}, \quad (9)$$

with saturation limits for recombination-type defects and shallow acceptors as, respectively,

$$N_\infty = (\alpha G^2/\beta C^2)^{1/3} \quad (10)$$

and

$$N_\infty = (\alpha n_i^4 \gamma^2/\beta)^{1/3}. \quad (11)$$

The annealing time, τ_a, remains the same as in Eq. (6), but the charge injection case now has cube root time dependence,

$$N = N_0 (1 + t/\tau)^{1/3} \quad \text{with } \tau = \frac{1}{3\beta}\left(\frac{N_0^3}{N_\infty^3 - N_0^3}\right). \quad (12)$$

Second-order reactions can also occur when lattice relaxations are driven by the energy released during electron-hole pair recombination. In this case, the forward reaction is driven by the np product [33],

$$\frac{dN}{dt} = \alpha A np - \beta N, \quad (13)$$

where p is the hole concentration and Anp is the nonradiative recombination rate. This model also produces $N \propto t^{1/3}$ behavior and is widely studied with respect to metastability in hydrogenated amorphous silicon [7].

III. METHODS

A. Device fabrication and characterization

Two sample types are evaluated: type 1 (standard) and type 2 (reduced sodium). The soda-lime glass substrate is cut, labeled, and cleaned prior to further processing. Type 2 samples had a sputtered AlO_x-AlN barrier layer (0.1 μm thick) to reduce the diffusion of sodium from the substrate. The molybdenum back contact layer (0.05 μm thick) is sputtered in an inline process for all samples in the same run. The subsequent CIGS layer (2–3 μm thick) is deposited in an inline coevaporation process and all samples are in the same CIGS run. The CdS buffer layer (0.05 μm thick) is deposited in batches by chemical bath deposition (CBD) according to standard procedures. The buffer-window stack is CBD CdS followed by sputtered undoped ZnO and Al-doped ZnO layers (0.15 μm thick total). The cells are completed with (Ni, Al)Ni grid contacts and the cell separation is by mechanical scribing. Each substrate contained ten solar-cell test structures. Average power conversion efficiencies are 16.2 and 12.9%

for type 1 and 2, respectively. Details on device fabrication and performance are provided in Ref. [34].

The type 2 CIGS layer is grown under reduced sodium conditions, which influences the gallium and band gap gradients. The barrier applied in type 2 cells is not as effective as had been demonstrated by previous tests. However, the expected trends of reduced efficiency and a flatter gallium gradient are apparent [34]. According to secondary ion mass spectroscopy data (not shown), the approximate average sodium content is 10^{19} cm^{-3} and 10^{18} cm^{-3} for type 1 and 2 devices, respectively.

B. Characterization and accelerated stress tests

J-V and C-V voltage sweeps are performed via a four-probe setup. J-V is measured with a Keithley 2400 source measure unit (SMU) in an ATLAS XXL+ chamber under dry conditions (<15% relative humidity), AM1.5G spectrum and 0.1 W/cm^2 illumination (Xe bulb source with spectral filters). C-V is measured with a Solartron SI 1260 A, which is a combination frequency generator and impedance analyzer. The peak-to-peak ac voltage is 0.28 V and the frequency is 10 kHz to 1 MHz. A resistance temperature detector (RTD) is placed on the device surface to monitor the temperature. Temperature control of cells at or near 25 °C is provided by a Julabo recirculating water chiller and heater.

Metastability is characterized by changes in J-V metrics determined by *in situ* current-voltage sweeps every 30 min under accelerated stress test (AST) conditions for a duration of 50–100 h. The stress and measurement systems are integrated in the ATLAS XXL+ chamber. Stress conditions are AM1.5G illumination of 0.1 W/cm^2 intensity, temperatures between 30 and 85 °C, and voltage biases at open-circuit ($V = V_{oc}$) and short-circuit ($V = 0$) conditions. Pre and poststress *ex situ* C-V measurements are also performed immediately before, within a few hours, and within a few days after stress. All *ex situ* measurements are conducted at room temperature.

C. Computational details

Spin-polarized density-functional-theory (DFT) calculations are performed with the Heyd-Scuseria-Ernzerhof (HSE06) screened hybrid functional [35] and projector augmented wave (PAW) method [36] as implemented in the VASP code [37,38]. The plane-wave energy cutoff energy is set to 455 eV. The fraction of Hartree-Fock exchange (α) in the HSE functional is set to 30%, which gives a band gap of 1.13 eV for $CuInSe_2$ and 1.72 eV for $CuGaSe_2$, close to the experimental values [39]. The $CuInSe_2$ and $CuGaSe_2$ systems are modeled using a large supercell containing 128 atoms. The standard supercell approach is employed to compute defect formation energies [40]. For charged defects, the electrostatic finite size error is corrected based on the correction scheme by Freysoldt, Neugebauer, and Van de Walle [41].

IV. RESULTS

A. Quantifying reaction kinetics

Light-, bias-, and heat-induced variations in doping are evident in Fig. 2, which shows the pre and poststress acceptor concentration (N) as a function of the p-n junction depletion width (W), (as typically derived from C-V data [42]) for six type 1 devices (type 2 results are similar but showed more drastic declines for the $V = 0$ stress cases). Devices stressed at $V = 0$ voltage bias (low charge injection) exhibited a trend of decreasing N with temperature. Contrarily, an increase in N is observed at $V = V_{oc}$ bias stress (high charge injection), but without apparent dependence on stress temperature. In fact, $T = 50\,^{\circ}C$ stress led to a greater increase in N than the higher temperatures. That may be indicative of the significant role of charge injection because although the cells are stressed at V_{oc} bias, the magnitude of V_{oc} (and therefore applied bias) decreased with temperature (by about 0.3%/K for CIGS devices) and varied with time. The time average value of V_{oc} (bias stress, $\overline{V}$) at each temperature is shown in Table I along with the initial, N_0, and final, N_f, acceptor concentrations. Since N varied with voltage, capacitance values from 0 to 0.5 V are used to determine the average N_0 and N_f, which provided reasonable values of doping in the depletion region.

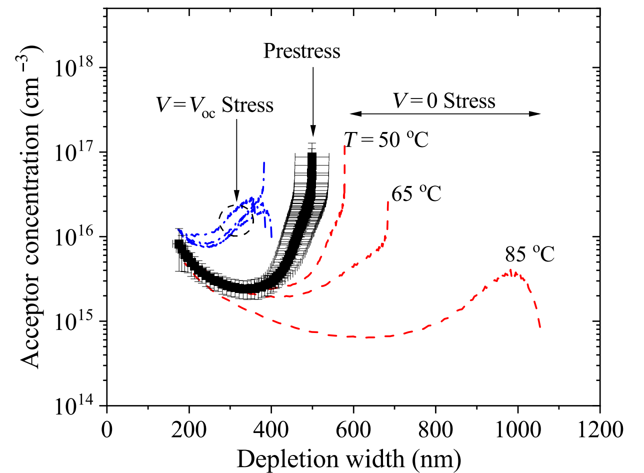

FIG. 2. Acceptor concentration versus depletion width for type 1 devices: six before stress testing (black points plus or minus one standard deviation error bars), three stressed at $V = V_{oc}$ bias (dash-dot, blue lines), and three stressed at $V = 0$ bias (dashed, red lines). Stress temperatures are shown for the $V = 0$ bias stress. The average value of voltage bias for each cell is shown in Table I.

TABLE I. Stress temperature (T), average voltage ($\overline{V}$), and time (t) for type 1 (typical sodium) and type 2 (reduced sodium) devices. Pre (N_0) and poststress (N_f) acceptor concentrations based on average of capacitance values from 0 to 0.5 V.

Type	T (°C)	$\overline{V}$ (mV)	t (h)	N_0 (10^{15} cm^{-3})	N_f (10^{15} cm^{-3})
1	50	0	100	4.9	5.0
1	65	0	100	4.6	2.1
1	85	0	30	4.9	1.2
1	50	652	100	6.1	14.5
1	65	634	100	7.0	12.8
1	85	593	63	8.1	11.8
2	50	0	100	4.9	3.3
2	65	0	100	5.5	1.0
2	85	0	43	4.0	0.5
2	50	618	100	8.2	16.6
2	65	596	100	7.2	12.7
2	85	541	45	5.5	5.4

Figure 2 indicates clear variations in shallow acceptor concentration during light or bias or heat stress that correlates well with V_{oc} drift. Open-circuit voltage as a function of time under stress up to 100 h is shown in Figs. 1(a) and 1(b) for cell types 1 and 2, respectively. Both cell types exhibited qualitatively similar behavior: increase in V_{oc} when stressed at $V = V_{oc}$ bias (high charge injection) and decrease in V_{oc} when stressed at short circuit conditions, $V = 0$ conditions (low charge injection). Similar to the acceptor density in Fig. 2, the V_{oc} reduction rate increased with temperature. The V_{oc} loss rate is clearly greater for type 2 (reduced sodium) devices. Other metrics, including short-circuit current and fill factor, are relatively stable compared to V_{oc}. Therefore, our analysis proceeds under the hypothesis that the LLR mechanism causes variations in shallow acceptors of density N to an observable degree. Hence, the appropriate saturation limit is given by Eqs. (5) or (11).

The time dependence of N is extracted from the $V_{oc}(t)$ data by noting that $V_{oc} \propto \ln N$. Fitting proceeded by first determining $\tau_a = 1/\beta$ from the low injection $V = 0$ stress cases by using Eq. (6) and the relation $V_{oc}(t)/V_{oc}(0) = \ln N/\ln N_0 = 1 - \beta t/\ln N_0$ to establish a linear fit. Initial values (N_0) are determined from the C-V data and are listed Table I. From an Arrhenius plot of β, the activation energy, E_β, and pre-exponential, β_0 are determined. Then, using the known value of β, the $V = V_{oc}$ early time stress data ($t \ll \tau_a$) are fit to determine τ (and therefore α) using the logarithm of Eq. (7) for first-order kinetics or Eq. (12) for second-order kinetics.

Figure 3(a) shows that type 2 devices tended to degrade more rapidly than type 1 devices under $V = 0$ light soak stress. Fitting the data with Eq. (6) yielded characteristic annealing times on the order of 10^4 to 10^6 s for both types; type 2 had shorter times. Saturation is typically not observed in the $V = 0$ bias cases, except for the type 2 device at $T = 85\,°$C, which saturated at about 15 h. The high-injection $V = V_{oc}$ stress cases shown in Fig. 3(b) indicate similar behavior and characteristic times for both device types. Fitting with first- and second-order kinetic Eqs. (7) and (12), respectively, provided similar results but second order fit the $V = V_{oc}$ stress data slightly better. Second-order fits are shown as the solid lines in Fig. 3(b). Whether first- or second-order kinetics are prevalent cannot be inferred from this analysis; further discussion is provided in Sec. V.

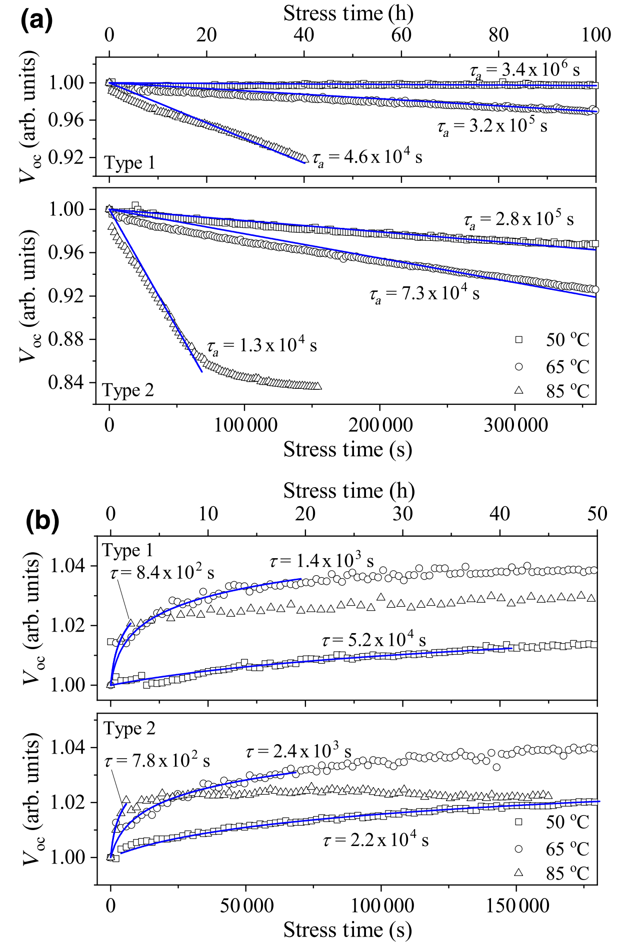

FIG. 3. Open-circuit voltage with time under stress at 0.1 W/cm^2 light intensity and voltage of (a) $V = V_{oc}$ and (b) $V = 0$ at the temperatures indicated. The characteristic annealing time is shown for each curve fit (lines) using the logarithm of Eq. (6) for (a) and Eq. (7) for (b).

Arrhenius plots for the forward (α) and backward (β) reaction rates are shown in Fig. 4 and the extracted activation energies and pre-exponential values are listed in Table II for first- and second-order kinetics (β is the same in both cases). Both forward and backward reaction rates are larger for type 2 devices (reduced sodium). Although Fig. 3(b) suggests that types 1 and 2 exhibited similar V_{oc} increase, we note that type 1 devices are subjected to

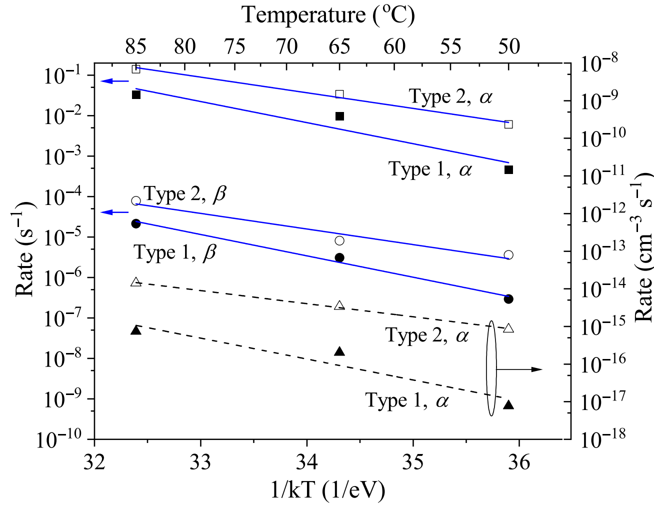

FIG. 4. Arrhenius plots of reaction rates α and β for type 1 and type 2 devices. Values for α are determined from first-order (fit with solid lines) and second-order (fit with dashed lines) kinetics. Arrhenius fit values are provided in Table II.

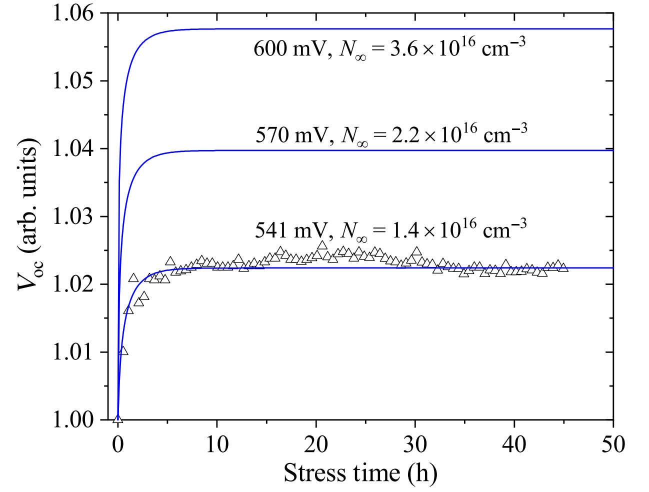

FIG. 5. V_{oc} versus time for the type 2 device stressed at 85 °C and $V = V_{oc}$ (points). Equation (9) and the relation $V_{oc} \propto \ln N$ at various applied bias are shown as curves along with the predicted saturation acceptor density, N_∞. Input values are listed in Tables I and II (last row).

higher voltage bias, as noted in Table I. Figures 3(a) and 3(b) indicate that sodium stabilizes doping in these CIGS devices.

The above calculated reaction rates are also used with Eq. (9) to fit the entire range of $V_{oc}(t)$ data. In Fig. 1, the model curves are based on the pre-exponentials from Table II for second-order kinetics. The activation energies from fitting all of the curves with Eq. (9) had mean values of $E_\alpha = 1.29$ eV and $E_\beta = 1.21$ eV for type 1 and $E_\alpha = 0.81$ eV and $E_\beta = 0.92$ eV for type 2, with standard deviations of $< \pm 0.04$ eV. Although this is a qualitative (by eye) fitting exercise, it demonstrates that the entire range of data can be fit with reaction rates close to the values in Table II. Note that in Eq. (2) for γ, the Fermi level splitting is given by $eU \approx \overline{V}$ from Table I for the V_{oc} bias cases. In the $V = 0$ bias case, γ is rather inconsequential for times prior to onset of saturation [cf. Eq. (6)] and can be set to zero. However, for the type 2 device stressed at $T = 85$ °C and $V = 0$, saturation is observed and the model curve in Fig. 1(b) is obtained with $eU = 0.25$ eV, resulting in $N_\infty = 2 \times 10^{13}$ cm^{-3}. The value of $eU = 0.25$ eV represents quasi-Fermi level splitting due to photoexcitation under short-circuit conditions.

The apparent nonmonotonic trend of saturation level with temperature in Fig. 3(b) is noteworthy. Although the 85 °C, $V = V_{oc}$ stress case had the most rapid initial increase, it exhibited a lower saturation level than the 65 °C case. That can be accounted for by the strong dependence of N_∞ on Fermi level splitting, $eU \approx \overline{V}$, which is lowest for the 85 °C case (see Table I). This point is illustrated in Fig. 5 where Eq. (9) is used to predict V_{oc} evolution and saturation densities at 85 °C for different voltage biases. The data for the type 2 device is shown by the points and all of the model curves use the appropriate values from Tables I and II (last row of both tables). A significant increase in N_∞ (and V_{oc}) is predicted with voltage bias.

B. First-principles calculations

To understand the microscopic origin of the observed metastability, we revisit the $(V_{Se} - V_{Cu})$ divacancy in $CuInSe_2$. As proposed earlier [19], the $(V_{Se} - V_{Cu})$ divacancy model in CIGS involves two predominant reactions

TABLE II. Pre-exponential values and activation energies extracted from the Arrhenius plots for both device types. (*) Units of α are (s^{-1}) for first-order and (cm^{-3} s^{-1}) for second-order kinetics. β is order independent.

Device type	Kinetics order	α_0 (*)	E_α (eV)	β_0 (s^{-1})	E_β (eV)
1	1	3.7×10^{15}	1.20 ± 0.36	3×10^{12}	1.22 ± 0.13
2	1	5.0×10^{11}	0.89 ± 0.09	2×10^{8}	0.89 ± 0.19
1	2	1.1×10^{3}	1.28 ± 0.39	3×10^{12}	1.22 ± 0.13
2	2	2.8×10^{-3}	0.80 ± 0.04	2×10^{8}	0.89 ± 0.19

due to electron (e) and hole (h) capture and emission [19],

$$(V_{\mathrm{Se}} - V_{\mathrm{Cu}})^{+} + e \rightleftharpoons (V_{\mathrm{Se}} - V_{\mathrm{Cu}})^{-} + h, \tag{14}$$

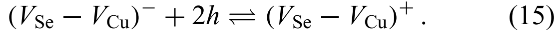

$$(V_{\mathrm{Se}} - V_{\mathrm{Cu}})^{-} + 2h \rightleftharpoons (V_{\mathrm{Se}} - V_{\mathrm{Cu}})^{+}. \tag{15}$$

The first reaction is electron capture (ec) in the forward direction and electron emission (ee) in reverse. The second reaction is hole capture (hc) in the forward direction and hole emission (he) in reverse. All four processes are mediated by thermal activation energies.

We compute the activation energies and the $(+/-)$ transition energy level of the $(V_{\mathrm{Se}} - V_{\mathrm{Cu}})$ complex for pure $\mathrm{CuInSe_2}$ (CIS) and $\mathrm{CuGaSe_2}$ (CGS) by using the HSE06 screened hybrid functional, which has been shown to yield a good description of the electronic and atomic structures and energetics in $\mathrm{Cu(In, Ga)Se_2}$. As shown in Fig. 6(a) for CIS, there are two distinct local minimum configurations for the $(V_{\mathrm{Se}} - V_{\mathrm{Cu}})$ complex. In the state L, two unsaturated In atoms are largely separated [denoted by the dashed line in Fig. 6(a)], while they form a dimer in the state S. According to the formation energy calculations shown in Fig. 6(b), the relative thermodynamic stabilities for these configurations vary depending on the charge state. For the state L, the positive charge state (+) is always more favorable than the neutral state (0) and no (+/0) charge transition level exists within the band gap. On the other hand, for the state S, the neutral state is the most stable when the Fermi level (E_F) is located very close to the valence-band maximum (VBM), while the negative charge state (−) becomes energetically more favorable than the neutral state when the Fermi level lies higher than 0.05 eV from the VBM. Also, it should be noted that there is no additional charge transition level, such as $(-/2-)$, within the band gap. This suggests that the state L and S serve as a shallow donor and acceptor, respectively. In Eqs. (14) and (15), the donor-type $(V_{\mathrm{Se}} - V_{\mathrm{Cu}})^{+}$ and acceptor-type $(V_{\mathrm{Se}} - V_{\mathrm{Cu}})^{-}$ correspond to the states L and S, respectively. The donor to acceptor transition $(+/-)$ occurs at $E_F = 0.37$ eV ($E_F = 0$ corresponds to VBM), indicating that this transition would require the thermal activation energy associated with structural relaxation as well as the capture of charge carriers.

As shown in Fig. 6(c), we compute the configuration coordinate diagram of the $(V_{\mathrm{Se}} - V_{\mathrm{Cu}})$ complex in its positive (+1), neutral (0), and negative (−1) charge states to estimate the energy required for structural change between the donor- and acceptor-type configurations. Starting from the lowest energy state, donor type $(V_{\mathrm{Se}} - V_{\mathrm{Cu}})^{+}$, capturing one electron could convert it to the acceptor type $(V_{\mathrm{Se}} - V_{\mathrm{Cu}})^{0}$ state. The energy required for this process (E_{ec}) is calculated to be 0.27 eV as listed in Table III. As a shallow acceptor, the acceptor type $(V_{\mathrm{Se}} - V_{\mathrm{Cu}})^{0}$ is likely ionized to $(V_{\mathrm{Se}} - V_{\mathrm{Cu}})^{-}$ by releasing one hole, which would increase the hole concentration as predicted in the reaction of Eq. (14). For the reverse reaction in Eq.

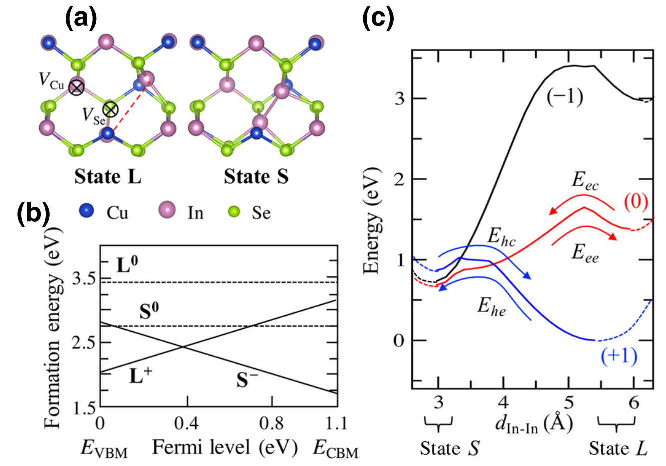

FIG. 6. (a) Optimized geometries of $V_{\mathrm{Se}} - V_{\mathrm{Cu}}$, (b) defect formation energies of $(V_{\mathrm{Se}} - V_{\mathrm{Cu}})$ complex under Se-rich growth condition as a function of the Fermi level, and (c) configuration coordinate diagram of $(V_{\mathrm{Se}} - V_{\mathrm{Cu}})$ complex in its positive (+1), neutral (0), and negative (−1) charge state for $\mathrm{CuInSe_2}$. In (c), all energies are computed relative to the energy of the donor-type $(V_{\mathrm{Se}} - V_{\mathrm{Cu}})^{+}$ complex and the respective relative energies correspond to $E_F = E_{\mathrm{VBM}}$. The parabolic curves are added (in dashed lines) beyond the equilibrium position for better understanding.

(15), the acceptor type $(V_{\mathrm{Se}} - V_{\mathrm{Cu}})^{-}$ can revert back to the donor type $(V_{\mathrm{Se}} - V_{\mathrm{Cu}})^{+}$ by capturing simultaneously two holes and overcoming the energy barrier (E_{hc}) of 0.16 eV. It should be mentioned that our computed energy barriers and E_{tr} in Table III are slightly different from those values reported earlier by Lany *et al.* [19]. The difference could be largely attributed to use of a different exchange-correlational functional that describes the electron-electron interaction in the system within the density-functional-theory calculations. In Ref. [19], they employed a local density approximation (LDA) [43], which gives inaccurate band gap of CIS (and CGS) and charge transition levels. Although they applied necessary energy corrections to fix errors originating from the LDA, they could not fix the inherent limitation of overbinding [44]. Due to the overly favorable bonding interaction, the energy gained by forming the In—In (or Ga—Ga) dimer in the acceptor-type configuration is likely overestimated. Indeed, for CIS in the positive charge state, the energy of the acceptor-type configuration is 0.8 eV less stable than that of the donor type from our hybrid calculation. However, the energy difference becomes much smaller to 0.3 eV with the LDA calculation. Such a tendency would likely underestimate E_{he}, while overestimating E_{hc}, as demonstrated in Table III. With the higher level of theory used here, we obtain more accurate energies and improve on the previously reported results [19] for the $(V_{\mathrm{Se}} - V_{\mathrm{Cu}})$ complex.

Based on the computed energy barriers in Table III, it is expected that the donor to acceptor and the acceptor

TABLE III. Calculated energy barriers for $CuInSe_2$ in eV from the configuration coordinate diagram in Fig. 6(c) and $(+1/-1)$ charge transition level E_{tr}. Corresponding activation energies and charge transition energy are also computed for $CuGaSe_2$. For reference, previously reported values for $CuInSe_2$ and $CuGaSe_2$ [19] are also listed.

	E_{ec}	E_{ee}	E_{hc}	E_{he}	E_{tr}
$CuInSe_2$	0.27	0.97	0.16	1.03	0.37
$CuGaSe_2$	0.46	0.73	0.14	1.56	0.61
Ref. [19]: $CuInSe_2$	~0.1	0.76	0.35	0.73	0.19
Ref. [19]: $CuGaSe_2$	0		0.28	0.92	0.32

to donor conversions would be dominated by an electron capture process in Eq. (14) and hole capture in Eq. (15), respectively. Also, it is expected that as Ga concentration increases, the transition from donor to acceptor would be less likely with the larger E_{ec}, while the transition from acceptor to donor would not change. While we compute accurate activation energies required for the transition between donor-type and acceptor-type configurations for CIS and CGS by using hybrid DFT functionals, the activation energies of CIGS, which could be approximated by averaging values from CIS and CGS, are still significantly smaller than what we obtain by fitting the experimental measurements (see Table II for E_α and E_β). This discrepancy suggests that the $(V_{Se} - V_{Cu})$ divacancy might not be responsible for the long-term metastability observed in this work.

V. DISCUSSION

The activation energy uncertainties in Table II are relatively large and could be improved by including additional measurements at each stress condition (work underway). We note that uncertainty is inherently large in this type of system. For example, our results indicate that the activation energies are sensitive to sodium content, which is difficult to control during polycrystalline film deposition. Furthermore, LLR phenomena are often associated with dispersive reaction kinetics due to distributions of activation energies [45,46].

A distinction between first- and second-order kinetics is not clear from the data because $V_{oc}(t)$ is proportional to the logarithm of Eq. (7) for first order and Eq. (12) for second order. As such, a factor of either 1/2 or 1/3 would be the difference. However, second-order kinetics did provide a slightly better fit to the data in Fig. 3(b). Further support for second-order kinetics comes from previous deep-level transient spectroscopy measurements that suggested negative-U center behavior [14] (a double charge capture process). Additional useful data would include doping concentration as a function of time and electro-optical techniques, such as photoinduced luminescence, absorption, and electron spin resonance.

Although the kinetic models do not specify the microscopic nature of the defects, they provide important guidance for evaluation of candidate defect species by additional experiments and *ab initio* calculations. Moving forward, the effects of alkali elements and oxygen on the $(V_{Se} - V_{Cu})$ divacancy and other defect complexes will be considered.

VI. CONCLUSIONS

The metastable behavior of CIGS PV devices is studied by means of *in situ* stress methods, reaction kinetics analysis, and first-principles calculations. Large lattice relaxations can account for both open-circuit voltage loss and gains depending on charge injection levels. Lattice relaxation activation energies extracted from the data are approximately 0.90 and 1.20 eV for devices with lower and higher sodium content, respectively. First-principles calculations suggest that the $(V_{Se} - V_{Cu})$ complex may not be responsible for the metastability observed here.

ACKNOWLEDGMENTS

Thanks to Dr. Hajime Shibata and the Compound Semiconductor Thin Film team at AIST, Tsukuba, Japan for fruitful discussions. This work is developed based upon funding from the Department of Energy Solar Energy Technology Office under Award No. DE-EE-0007750. Part of this work is performed under the auspices of the U.S. Department of Energy at Lawrence Livermore National Laboratory under Contract No. DE-AC52-07NA27344.

[1] D. Redfield and R. H. Bube, *Photo-Induced Defects in Semiconductors* (Cambridge University Press, Cambridge, 2006), Vol. 4.

[2] C. H. Henry and D. V. Lang, Nonradiative capture and recombination by multiphonon emission in GaAs and GaP, Phys. Rev. B **15**, 989 (1977).

[3] G. A. Baraff and M. A. Schluter, Electronic aspects of the optical-absorption spectrum of the EL2 defect in GaAs, Phys. Rev. B **45**, 8300 (1992).

[4] H. C. Wright, R. J. Downey, and J. R. Canning, Conductivity storage in CdS, J. Phys. D: Appl. Phys. **1**, 1593 (1968).

[5] H. Yin, A. Akey, and R. Jaramillo, Large and persistent photoconductivity due to hole-hole correlation in CdS, Phys. Rev. Mater. **2**, 084602 (2018).

[6] M. R. Lorenz, B. Segall, and H. H. Woodbury, Some properties of a double acceptor center in CdTe, Phys. Rev. **134**, A751 (1964).

[7] D. L. Staebler and C. R. Wronski, Reversible conductivity changes in discharge-produced amorphous Si, Appl. Phys. Lett. **31**, 292 (1977).

[8] K. Bothe, R. Sinton, and J. Schmidt, Fundamental boron-oxygen-related carrier lifetime limit in mono-and

multicrystalline silicon, Prog. Photovoltaics: Res. Appl. **13**, 287 (2005).

[9] L. Huang, C.-C. Lin, M. Riediger, R. Röder, P. L. Tse, C. Ronning, and J. G. Lu, Nature of AX centers in antimony-doped cadmium telluride nanobelts, Nano Lett. **15**, 974 (2015).

[10] A. Nagaoka, D. Kuciauskas, J. McCoy, and M. A. Scarpulla, High p-type doping, mobility, and photocarrier lifetime in arsenic-doped CdTe single crystals, Appl. Phys. Lett. **112**, 192101 (2018).

[11] M. A. Green, Y. Hishikawa, E. D. Dunlop, D. H. Levi, J. Hohl-Ebinger, and A. W. Ho-Baillie, Solar cell efficiency tables (version 52), Prog. Photovoltaics: Res. Appl. **26**, 427 (2018).

[12] T. Meyer, F. Engelhardt, J. Parisi, and U. Rau, Spectral dependence and Hall effect of persistent photoconductivity in $Cu(In, Ga)Se_2$ polycrystalline thin films, J. Appl. Phys. **91**, 5093 (2002).

[13] M. N. Ruberto and A. Rothwarf, Time-dependent open-circuit voltage in $CuInSe_2/CdS$ solar cells: Theory and experiment, J. Appl. Phys. **61**, 4662 (1987).

[14] M. Igalson and H. W. Schock, The metastable changes of the trap spectra of $CuInSe_2$-based photovoltaic devices, J. Appl. Phys. **80**, 5765 (1996).

[15] U. Rau, M. Schmitt, J. Parisi, W. Riedl, and F. Karg, Persistent photoconductivity in $Cu(In, Ga)Se_2$ heterojunctions and thin films prepared by sequential deposition, Appl. Phys. Lett. **73**, 223 (1998).

[16] S. J. Heise, V. Gerliz, M. S. Hammer, J. Ohland, J. Keller, and I. Hammer-Riedel, Light-induced changes in the minority carrier diffusion length of $Cu(In, Ga)Se_2$ absorber material, Solar Energy Mater. Solar Cells **163**, 270 (2017).

[17] J. Nishinaga, T. Koida, S. Ishizuka, Y. Kamikawa, H. Takahashi, M. Iioka, H. Higuchi, Y. Ueno, H. Shibata, and S. Niki, Effects of long-term heat-light soaking on $Cu(In, Ga)Se_2$ solar cells with KF postdeposition treatment, Appl. Phys. Express **10**, 092301 (2017).

[18] J. Nishinaga, T. Nagai, T. Sugaya, H. Shibata, and S. Niki, Single-crystal $Cu(In, Ga)Se_2$ solar cells grown on GaAs substrates, Appl. Phys. Express **11**, 082302 (2018).

[19] S. Lany and A. Zunger, Light-and bias-induced metastabilities in $Cu(In, Ga)Se_2$ based solar cells caused by the $(V_{Se} - V_{Cu})$ vacancy complex, J. Appl. Phys. **100**, 113725 (2006).

[20] M. Igalson, P. Zabierowski, D. Przado, A. Urbaniak, M. Edoff, and W. N. Shafarman, Understanding defect-related issues limiting efficiency of CIGS solar cells, Solar Energy Mater. Solar Cells **93**, 1290 (2009).

[21] J. Serhan, Z. Djebbour, W. Favre, A. Migan-Dubois, A. Darga, D. Mencaraglia, N. Naghavi, G. Renou, J.-F. Guillemoles, and D. Lincot, Investigation of the metastability behavior of CIGS based solar cells with ZnMgO–Zn(S,O,OH) window-buffer layers, Thin Solid Films **519**, 7606 (2011).

[22] M. Burgelman, K. Decock, S. Khelifi, and A. Abass, Advanced electrical simulation of thin film solar cells, Thin Solid Films **535**, 296 (2013).

[23] F. Obereigner, N. Barreau, W. Witte, and R. Scheer, Open-circuit and doping transients of $Cu(In, Ga)Se_2$ solar cells with varying Ga content, J. Appl. Phys. **117**, 055704 (2015).

[24] M. Maciaszek and P. Zabierowski, Quantitative analysis of the persistent photoconductivity effect in $Cu(In, Ga)Se_2$, J. Appl. Phys. **123**, 161404 (2018).

[25] A. Urbaniak and M. Igalson, Creation and relaxation of light-and bias-induced metastabilities in $Cu(In, Ga)Se_2$, J. Appl. Phys. **106**, 063720 (2009).

[26] H. Okada and T. Minemoto, Characterization method for the relaxation process of metastable defect states in $Cu(In, Ga)Se_2$ thin films with photoisothermal capacitance transient spectroscopy, Jpn. J. Appl. Phys. **50**, 020203 (2011).

[27] I. Khatri, K. Shudo, J. Matsuura, M. Sugiyama, and T. Nakada, Impact of heat-light soaking on potassium fluoride treated CIGS solar cells with CdS buffer layer, Prog. Photovoltaics: Res. Appl. **26**, 171 (2018).

[28] S. Ishizuka, H. Shibata, J. Nishinaga, Y. Kamikawa, and P. J. Fons, Effects of RbF postdeposition treatment and heat-light soaking on the metastable acceptor activation of $CuInSe_2$ thin film photovoltaic devices, Appl. Phys. Lett. **113**, 063901 (2018).

[29] R. Harju, V. G. Karpov, D. Grecu, and G. Dorer, Electron-beam induced degradation in CdTe photovoltaics, J. Appl. Phys. **88**, 1794 (2000).

[30] S. Lany and A. Zunger, Intrinsic DX Centers in Ternary Chalcopyrite Semiconductors, Phys. Rev. Lett. **100**, 016401 (2008).

[31] D. J. Chadi and K.-J. Chang, Self-compensation through a large lattice relaxation in p-type ZnSe, Appl. Phys. Lett. **55**, 575 (1989).

[32] S.-H. Wei and S. B. Zhang, Chemical trends of defect formation and doping limit in II-VI semiconductors: The case of CdTe, Phys. Rev. B **66**, 155211 (2002).

[33] M. Stutzmann, W. B. Jackson, and C. C. Tsai, Light-induced metastable defects in hydrogenated amorphous silicon: A systematic study, Phys. Rev. B **32**, 23 (1985).

[34] M. Nardone, Y. Patikirige, C. Walkons, S. Bansal, T. M. Friedlmeier, K. E. Kweon, J. B. Varley, and V. Lordi, in *Baseline Models for Three Types of CIGS Cells: Effects of Buffer Layer and* Na *Content* (IEEE, Waikoloa, HI, 2018).

[35] J. Heyd, G. E. Scuseria, and M. Ernzerhof, Hybrid functionals based on a screened Coulomb potential, J. Chem. Phys. **118**, 8207 (2003).

[36] P. E. Blöchl, Projector augmented-wave method, Phys. Rev. B **50**, 17953 (1994).

[37] G. Kresse and J. Furthmüller, Efficiency of ab-initio total energy calculations for metals and semiconductors using a plane-wave basis set, Comput. Mater. Sci. **6**, 15 (1996).

[38] G. Kresse and J. Furthmüller, Efficient iterative schemes for ab initio total-energy calculations using a plane-wave basis set, Phys. Rev. B **54**, 11169 (1996).

[39] G. E. H. Moussa, F. Guastavino, and C. Llinares, Band gap of $CuInSe_2$ thin films fabricated by flash evaporation determined from transmission data, J. Mater. Sci. Lett. **21**, 215 (2002).

[40] C. Freysoldt, B. Grabowski, T. Hickel, J. Neugebauer, G. Kresse, A. Janotti, and C. G. Van de Walle, First-principles calculations for point defects in solids, Rev. Mod. Phys. **86**, 253 (2014).

[41] C. Freysoldt, J. Neugebauer, and C. G. Van de Walle, Electrostatic interactions between charged defects in supercells, Phys. Status Solidi (b) **248**, 1067 (2011).
[42] D. K. Schroder, *Semiconductor Material and Device Characterization* (John Wiley & Sons, New York, 2006).
[43] W. Kohn and L. J. Sham, Self-consistent equations including exchange and correlation effects, Phys. Rev. **140**, A1133 (1965).
[44] A. Van de Walle and G. Ceder, Correcting overbinding in local-density-approximation calculations, Phys. Rev. B **59**, 14992 (1999).
[45] K. Shimakawa, Persistent photocurrent in amorphous chalcogenides, Phys. Rev. B **34**, 8703 (1986).
[46] R. J. Freitas and K. Shimakawa, Kinetics of persistent photoconductivity in crystalline III-V semiconductors, Philos. Mag. Lett. **97**, 257 (2017).